High Speed Time-Domain Imaging

Shingo Mandai and Edoardo Charbon

Abstract The chapter focuses on positron emission tomography (PET), a medical imaging technique that combines high speed with high complexity data processing. In PET, optical sensors detect gamma events generated by the annihilation of an electron and a positron, by measuring hundreds of individual photon times-of-arrival. These measurements are carefully analyzed, every 6.4 μs, by ultra-fast networks and distributed reconstruction algorithms, all running in parallel at several gigabit-per-second. In this context, we present an array of 4 × 4 digital silicon photomultipliers (MD-SiPMs) integrated in standard CMOS, capable of capturing and digitizing up to 32 million individual photon times-of-arrival per second, for up to 0.6 million gamma events per second. For each gamma event the equivalent energy is also computed to help the reconstruction algorithms screen out noise. The sensor is the core of the world's first endoscopic digital PET, a tool with unprecedented levels of contrast and detail for early and accurate cancer diagnostics.

1 Introduction

1.1 Medical Imaging

In nuclear medicine, small amounts of radio-isotopes are used to diagnose and localize several ailments, including cancer, heart disease, gastrointestinal, endocrine, and neurological disorders, and other abnormalities found in our organism. There exist a variety of diagnostic technique in nuclear medicine. Scintigraphy is a

S. Mandai (✉) · E. Charbon
Faculty of Electrical Engineering, TU Delft, Delft University of Technology, Mekelweg 4, 2628 CD Delft, The Netherlands
e-mail: s.mandai@tudelft.nl

P. Harpe et al. (eds.), *High-Performance AD and DA Converters, IC Design in Scaled Technologies, and Time-Domain Signal Processing*,
DOI: 10.1007/978-3-319-07938-7_13,

two-dimensional (2-D) imaging technique, while Single Photon Emission Computed Tomography (SPECT) and Positron emission tomography (PET) are three-dimensional (3-D) tomographic techniques. The most important advantage of PET imaging over SPECT is that it can obtain images with a much higher sensitivity (by approximately two to three orders of magnitude); i.e. due to the capability of collecting a higher percentage of the emitted events [1, 2]. Before conducting a PET scan, a radiopharmaceutical, which is a short-lived radioactive tracer isotope, is injected into a patient. The tracer is combined into a biologically active molecule that is absorbed selectively in tissues of interest. As the radioisotope undergoes positron emission decay (also known as positive beta decay), it emits a positron, an antiparticle of the electron with opposite charge. The emitted positron travels in the tissue for a short distance, which is typically less than 1 mm, before it annihilates with an electron available in the surrounding medium. After the annihilation, a pair of gamma photons is produced with approximately opposite directions (180°) as shown in Fig. 1. The coincident gamma photons are detected when they reach a scintillator in the detector ring, creating a burst of visible light which is detected by photomultiplier tubes (PMTs) or silicon based photon sensors. After collecting tens of thousands of coincidence events along with straight lines, known as lines of response (LORs), it is possible to localize their source using appropriate reconstruction algorithms. Photons that are not detected in coincidence (i.e. within a coincident timing window of a few nanoseconds) are ignored.

1.2 Radiation Coincident Detection and Timing Resolution

Radiation detection systems are a key component of any imaging system. The radiation detection system is composed of a scintillation material (scintillator) and photo sensors as shown in Fig. 1. The scintillation material converts high-energy photons into visible light which can be detectable with a conventional photo sensor. The integral of the visible photons is proportional to the total energy deposited in the detector by the radiation. The timing resolution of a PET detector corresponds to the statistical timing fluctuations or uncertainty due to the timing characteristics of scintillator and photo sensor. Figure 2 shows the coincident detection of two detectors. The output from each detector is discriminated by a certain threshold from detector noise or scattered gamma events which have low energy, and sent to a data acquisition system (DAQ). Since the timing resolution represents the variability in the signal arrival times (time-of-arrival, TOA) for different events, it needs to be properly measured for detecting coincident events to distinguish true events from false events.

The accuracy of the coincidence detection is defined as coincidence time resolution (CTR), as shown in Fig. 2. Good timing resolution of a PET detector, besides helping reduce the number of random coincidences, can also be used to estimate the annihilation point between the two detectors by measuring the arrival time

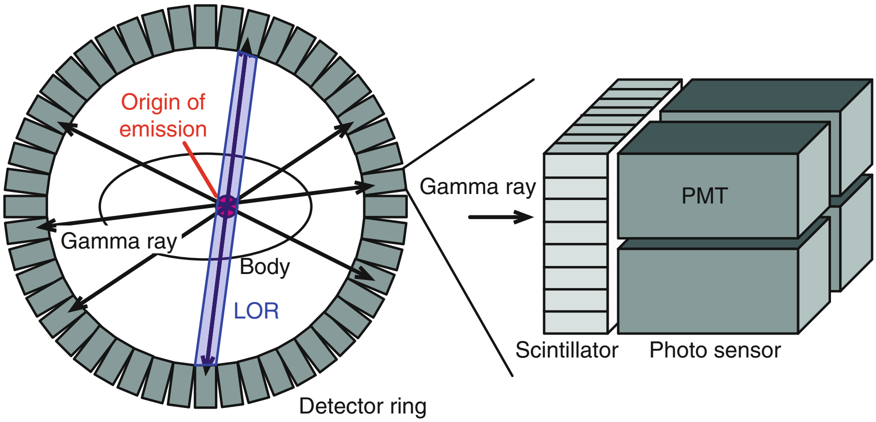

Fig. 1 Structure of PET scanner

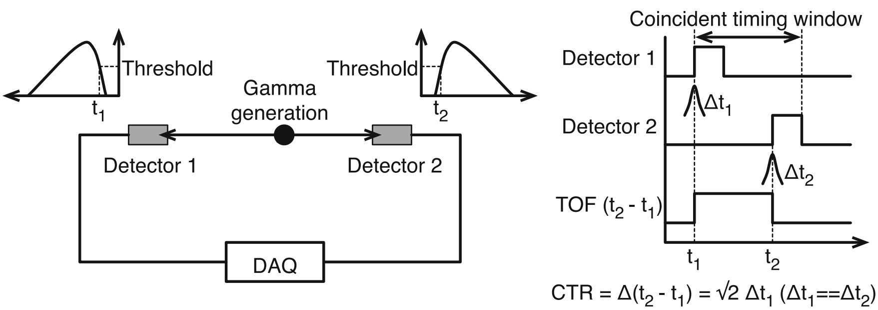

Fig. 2 Detecting coincident events in two detectors

difference of the two gamma photons. This PET scanner is called time-of-flight PET (TOF PET) [3–5]. The advantage of estimating the location of the annihilation point is the improved signal-to-noise ratio (SNR) obtained in the acquired image, arising from a reduction in noise propagation during the image reconstruction process. Figure 3 shows the comparison between non TOF PET and TOF PET. The constructed picture by TOF PET will be sharper with higher contrast.

1.3 Photo Sensors

Photo sensors are coupled to a scintillator using a glue that maximizes the detectability of visible photons generated in the scintillator upon a gamma event. The goal is to collect as many photons as possible with the accurate TOA

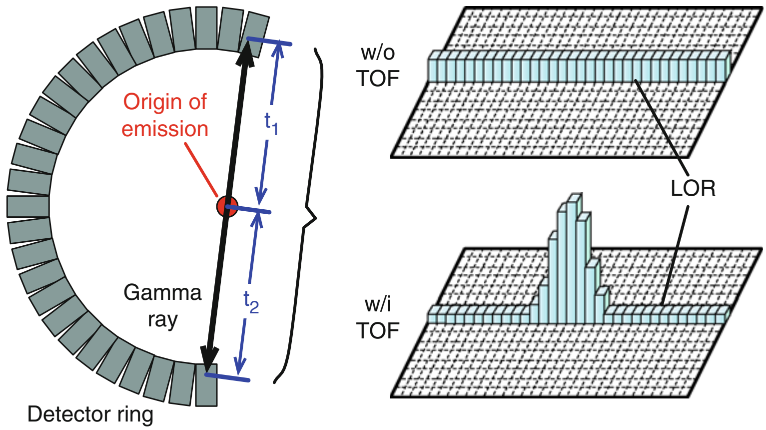

Fig. 3 Advantage of TOF PET

acquisition of gamma photons. SiPMs are a valid solid-state alternative to PMTs because of their robustness to magnetic fields, compactness, and low bias voltage [6]. SiPMs consist of an array of avalanche photodiodes operating in Geiger mode (single-photon avalanche diodes, SPADs). In SPADs, the absorbed light generates an electron-hole that may trigger an avalanche. Two flavors exist for SiPMs: analog and digital. An analog SiPM (A-SiPM) is composed of an array of SPADs, whose avalanche currents are summed in one node, and the output is processed with off-chip components as shown in Fig. 4a [6–12]. In digital SiPMs (D-SiPMs) on the contrary, all of the SPAD digital outputs are combined together by means of a digital OR, and the output is directly routed to an on-chip time-to-digital converter (TDC) to reduce external components and temporal noise as shown in Fig. 4b [13–17].

2 Analysis of Timing Resolution and Proposal for a Sensor Architecture

2.1 Modeling Scintillations

For the emitted photons from a LYSO scintillator, we can assume that detection occurs at time, θ as shown in Fig. 5. The time information of each photon can be considered as statistically independent and identically distributed (i.i.d.) following a probability density function (p.d.f.), which has been modeled as a double-exponential with rise time t_r and decay time t_d [18] $f(t|\theta) = (\exp(-\frac{t-\theta}{t_d}) - \exp(-\frac{t-\theta}{t_r}))/(t_d - t_r)$ when t $>$ θ, otherwise, $f(t|\theta) = 0$. Upon photon impingement, the SPAD jitter and an electrical jitter are convolved with the scintillator-based p.d.f., $f_{emi}(t|\theta)$. The dark counts follow an exponential probability distribution with

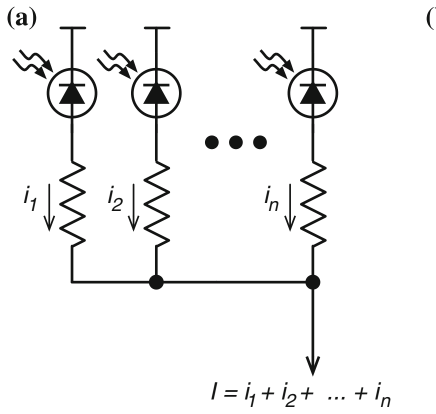

Fig. 4 Configuration of **a** A-SiPMs and **b** D-SiPMs

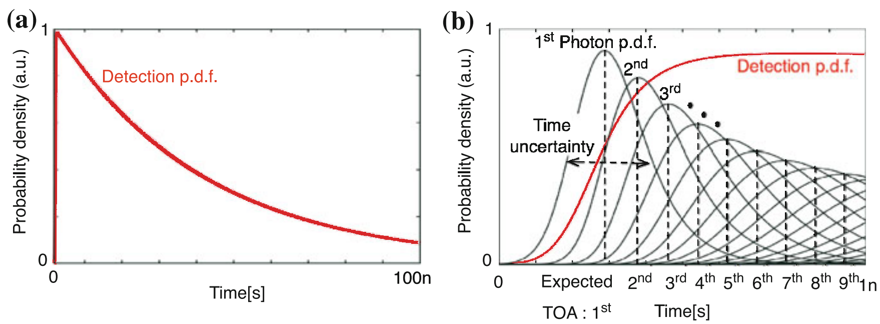

Fig. 5 **a** Detection p.d.f. **b** p.d.f. of the k-th primary photon detected after the first detected photon

event rate, λ, also known as dark count rate (DCR), and reset time, t_r, as $f(t) = \lambda \exp(-\lambda(t - t_r))$ when $t > t_r$, otherwise, $f(t) = 0$. The p.d.f. of the dark counts should also be convolved with an electrical jitter to be $f_{dcr}(t|t_r)$. The detection cycle, or frame, starts at the earliest before θ and it lasts a frame period, T. Thus the dark count p.d.f. is summed up for each reset time and then normalized. The scintillator-based p.d.f. and the dark count p.d.f. are mixed with mixing ratio $\alpha : (1 - \alpha)$ where α is defined by the percentage of photons emitted from scintillator, N, out of total detectable events, $N + \lambda T$, as,

$$f_{emi+dcr}(t|\theta) = \alpha f_{emi}(t|\theta) + (1 - \alpha) \frac{\int_{\theta-T}^{\theta} f_{dcr}(t|tr)\, dr}{\int_{\theta-T}^{\theta} \int_{t_r}^{\infty} f_{dcr}(t|tr)\, dt\, dr}.$$

Finally, the mixed p.d.f. is used for calculating the Fisher information [19] for the rth-order statistics p.d.f. or the joint p.d.f. for the first r-order statistics, then the Crámer-Rao lower bound for the unbiased estimator, θ, is calculated.

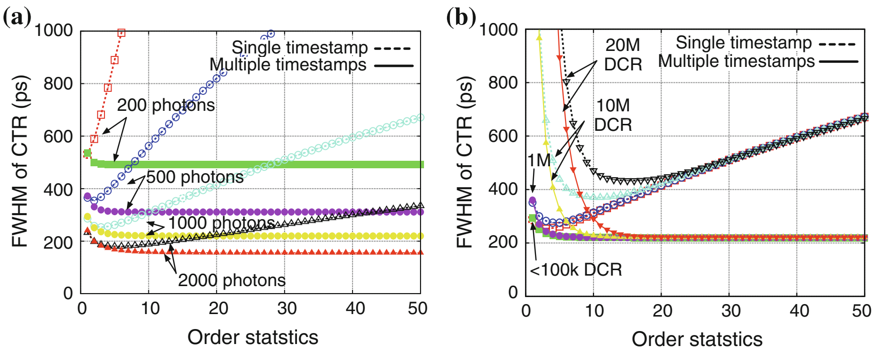

Fig. 6 Order statistics with a single timestamp or multiple timestamps v.s. FWHM of timing resolution: **a** various number of detected photons, 200, 500, 1000, and 2000 at 1 Hz DCR (which is almost negligible), **b** various values of DCR, less than 1,10, 20 MHz at 1000 detected photons

In our SPADs, we assumed normal jitter distributions with a standard deviation of 100 ps, the rise and decay times of a LYSO scintillator are 200 ps and 40 ns, respectively, while the number of detected photons is varied from 100 to 5,000, and DCR varied from 1 to 100 MHz. Figure 6 shows the relation between order statistics and full-width-at-half-max (FWHM) timing resolution. Figure 6a shows that the timing resolution improves with multiple timestamps. Furthermore, the timing resolution with multiple timestamps doesn't degrade due to DCR while the timing resolution with a single timestamp degrades with certain amount of DCR, as shown in Fig. 6b. The FWHM with multiple timestamps improves 13 % if compared to the FWHM with a single timestamp at less than 100 kHz DCR, however, the FWHM is 20 and 40 % better at 1 and 10 MHz DCR, respectively. From this work, it is clear that D-SiPMs capable of providing multiple timestamps are useful not only to improve timing resolution but especially to ensure tolerance to DCR and independence from a threshold and from the energy of the gamma event.

2.2 Multi-Channel Digital Silicon Photomultipliers

The ideal D-SiPM, as shown in Fig. 7a, gives minimum single-photon timing resolution (SPTR) by minimizing the skew, and achieves the statistical approach to estimate TOA by detecting TOAs of multiple photons in a single gamma event. However, the main drawback of the approach proposed in [20] is a low fill factor due to the need for significant silicon real estate to implement per-pixel functionality. In order to keep high PDE, 3-D integration is a promising technique. However, current 3D IC technologies are still expensive and hard to get. To achieve both high fill factor and acquisition of multiple timestamps, a new type of D-SiPM has been proposed [21–23]. Sharing one TDC with several pixels has the advantage of increasing the fill factor while still enabling somewhat independent

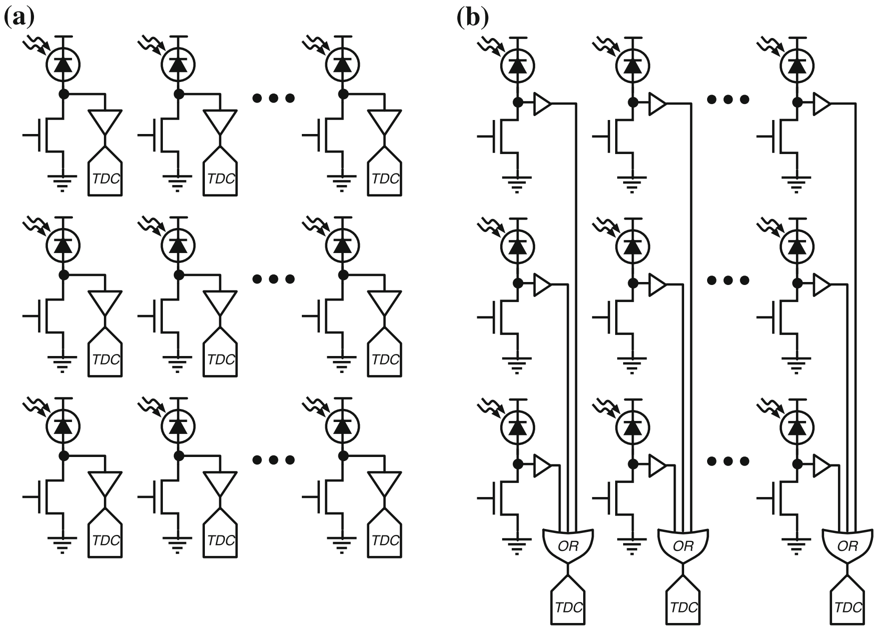

Fig. 7 **a** Ideal D-SiPM. **b** Proposed MD-SiPM

photon TOA evaluation, as shown in Fig. 7b. The skew problem is also improved when compared to conventional D-SiPMs for single-photon detection, and the multiple timing information can be utilized in a statistical approach for multiple-photon detection. This type of SiPMs is called multi-channel digital SiPM, or MD-SiPM. The MD-SiPM can achieve both high fill factor and enough multiple timestamps to improve timing resolution using the same principles outlines earlier.

3 Proposed SiPM Architecture

3.1 SiPM Configuration

Figure 8 shows the proposed MD-SiPM array configuration. Each SiPM in the array comprises 416 photo-detecting cells and measures 800 × 780 μm^2, adapted to the crystal dimensions. A 20 m gap enables adequate glue reflow in the pixelation process. Each pixel measures 50 × 30 μm; it generates a sharp pulse in correspondence to a photon detection that is routed directly to a TDC. Adjacent pixels are routed to independent TDCs by triples (every three pixels, the TDC is reused); this approach prevents misses in closely striking photons, thereby reducing local saturation. There are 48 TDCs per SiPM column, each operating

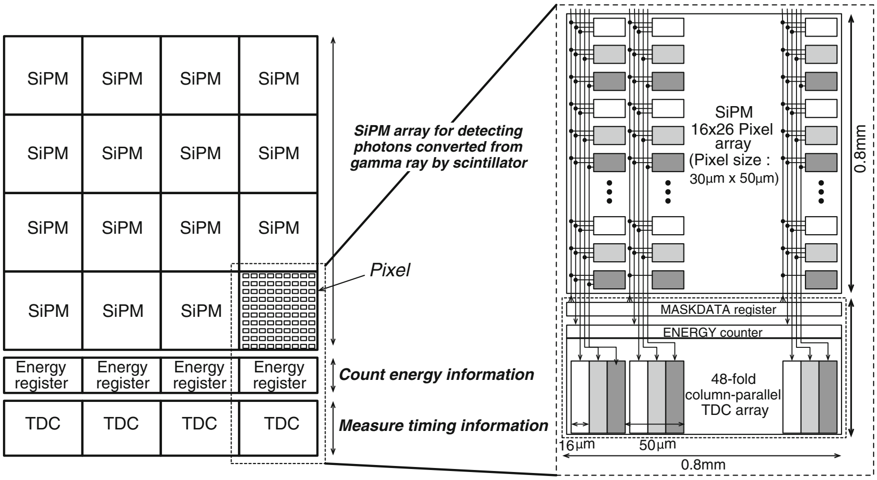

Fig. 8 Block diagram of the proposed sensor capable of detecting a large number of photons and their times-of-arrival with picosecond accuracy

simultaneously with a LSB duration of 44 ps. The number of photons, and thus the energy of the gamma event, is proportional to the number of triggered pixels. Thus, after each event the triggered pixels are counted; the corresponding digital code (1 or 0) is read out along with the complete statistical profiles of the projected photons, and summed up to calculate the total number of photons in one SiPM. Even though the number of cells is 416, it is possible to utilize saturation correction to count more than the number of cells [24]. To minimize photon misses, the array was designed with a fill factor up to 57 %. In our application, the pitch of the SiPMs is 800 μm, so as to match the 800 × 800 μm^2 section of the individual crystal in a pixelated scintillator. So the overall fill factor is equivalent to the fill factor of one pixel. To minimize dark counts in a SiPM, a masking procedure is used. Masking an SiPM consists of depriving it from a certain number of SPADs whose activity exceeds a threshold, also known as screamers. The MASKDATA register is used for disabling those pixels with DCR exceeding a threshold, so as to minimize spurious TDC activation. The ENERGY register is used for reading out the number of pixels that detected at least a photon.

3.2 Pixel Architecture

Figure 9a shows the schematic of a pixel; it comprises the SPAD, a 1-bit counter for energy estimation, a masking circuit, and a pulse shaper /column driver. The frame will start after RST resets the SPAD. When a shower of photons is generated in the scintillator, one of them may hit the SPAD in the pixel, generating a digital

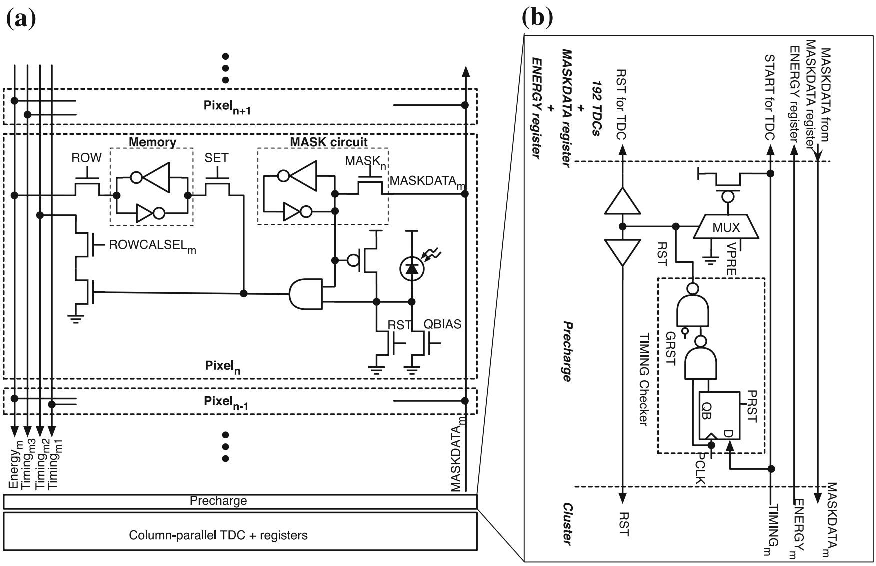

Fig. 9 **a** The pixel architecture comprises a SPAD, a 1-bit counter for energy estimation, a memory for masking, active and passive quenching, and a column driver circuit. **b** Detail of the pre-charge structure implemented at the bottom of the array

pulse to pull-down TIMING$_m$. QBIAS controls the quenching resistance of the SPAD and controls the digital pulse width to be more than the frame period. The event triggers the 1-bit counter, and it is read out as ENERGY$_m$ by ROW after latching the 1-bit counter value by SET. Masking is carried out in advance row-by-row, using signals MASKDATA$_m$ and ROWCALSEL, by bringing the SPAD bias below breakdown and by disabling the signal generated at its anode.

3.3 Readout Architecture from MD-SiPMs to Column-Parallel TDC Bank

Figure 9b shows the schematic of the pre-charge circuit used at the bottom of each column, which is terminated by a TDC. This circuit is used to prepare a TDC for a photon hit by employing signal GRST. TIMING$_m$ is pre-charged during RST for pixels and TDCs; this signal is asserted every 6.4 μs via signal GRST. PCLK is also causing a reset for pixels and TDCs when the number of firing TDCs exceeds a threshold within a pre-determined time, say 100 ns. This early reset mechanism, known as *smart reset* is performed so as to prevent gamma event misses when TDCs are occupied recording previous background photons or noise. VPRE is used to control the pull-up resistance for TIMING$_m$, and TIMING$_m$ used as

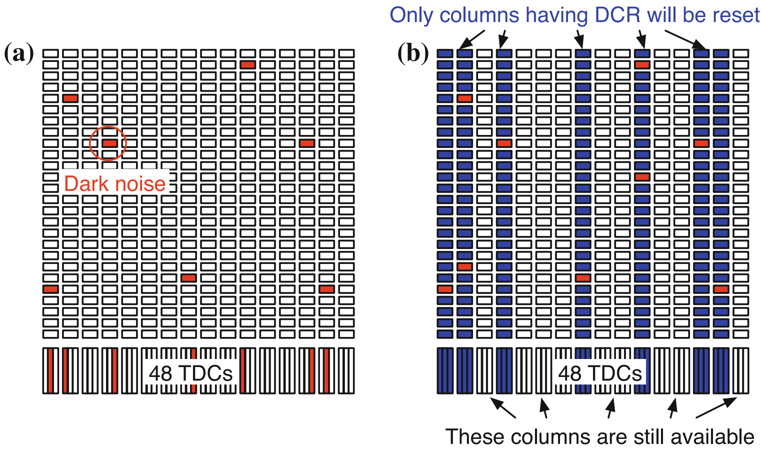

Fig. 10 Principle of smart reset. **a** Pixel and TDC occupation due to dark count noise as an example. **b** The columns that will be reset by *smart reset* in the example

START signals for TDC. Figure 10 shows how *smart reset* is carried out. Figure 10a shows the pixels who had dark count noise and TDCs consequently activated. During the *smart reset*, the blue colored column pixels and TDCs fired due to dark count noise are reset as shown in Fig. 10b, the rest of the column pixels and TDCs are thus available for a gamma event. Conventionally, SiPMs employ an event driven readout because the gamma event is classified as random coincidence. However, D-SiPMs take more than 600 ns to correct and read out the data [17], which is assumed as the dead time, while analog SiPMs take much shorter time. By employing the frame based readout, the data can be read out in the background to reduce dead time. Figure 11 shows the timing diagram of 6.4 s frame based readout. At the beginning of each frame, all the SPADs in every MD-SiPM are reset globally by GRST, and then every 60 ns, the *smart reset* is applied. The number of firing TDCs starts increasing due to dark counts, even in the absence of gamma events. By *smart reset*, pixels and TDCs are reset by PCLK. Upon occurrence of a gamma event, many TDCs fire in a short period ($\leq$100 ns) and the number of firing TDCs exceeds a threshold, thus preventing assertion of PCLK until the end of the frame. At the end of the frame, the pixel data are sent to the pixel memories and the TDC data are latched to TDC registers by SET. These data are read out, during which time the MD-SiPMs start the next frame.

3.4 Column-Parallel TDC Bank

In this MD-SiPM array, a column-parallel TDC utilizing a common VCO has been proposed to mitigate LSB variations. Figure 12 shows the architecture and a simple timing diagram of the proposed column-parallel TDC with a common VCO.

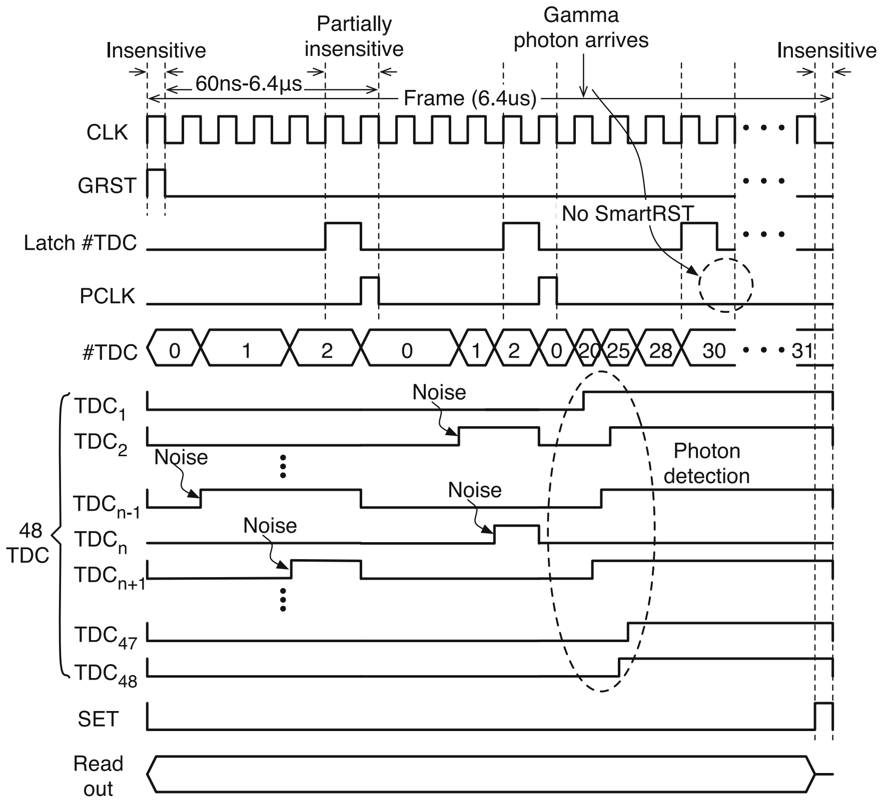

Fig. 11 Timing diagram for frame based readout

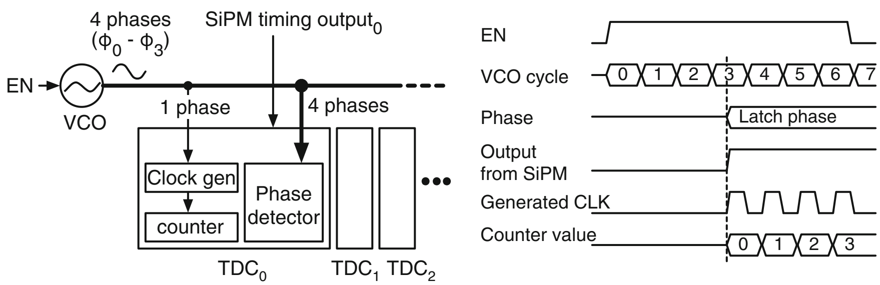

Fig. 12 Architecture of the proposed column-parallel TDC with a common oscillator. On the *right* the logic control timing diagram is shown

A TDC consists of a phase detector, a clock generator, and a counter. The VCO starts to propagate 4 phases, $\phi_0 - \phi_3$ (45 degrees of phase), after EN is asserted high. When the TDC receives a trigger from an MD-SiPM, the phase is latched by the phase detector while the clock for the counter is enabled by the clock generator. 192 TDCs have been implemented in the first version of the column-parallel TDC utilizing a common VCO.

Figure 13a shows one TDC schematic including the phase detector as a fine conversion and a counter as a coarse conversion. The coarse conversion is achieved by counting the clock cycles from the assertion of START (SPAD firing on the corresponding column) to the end of the frame (STOP signal) using the 12-bit counter; the LSB of this conversion is 1.4 ns. In the phase detection, upon START assertion, the phases from the VCO are latched by two-phase detectors with slightly skewed signals, ENB_1 and ENB_2. The small skew is realized by implementing two different inverter chains biased differently and calibrated to have an optimized skew for the best DNL. Figure 13b shows the VCO schematic; the VCO is activated at the beginning of the frame by enabling the ring oscillation and stopped at the end of the frame to save power. Figure 13c shows the bandgap voltage reference circuit for the VCO and the inverter chain in the TDC to ensure stable frequency generation and delay control on the chip. The VCO frequency and delay of the inverter chain in the TDC may also be conveniently programmed.

Figure 14a shows the timing diagram after EN becomes high. The phase starts to propagate while EN is high, and it is latched when EN becomes low. Figure 15b shows the phase detection of the proposed phase detector. Conventionally, the phase detector looks only at ϕ_0 and $\overline{\phi_0}$, ϕ_1 and $\overline{\phi_1}$, ϕ_2 and $\overline{\phi_2}$, and ϕ_3 and $\overline{\phi_3}$, resulting in 8 phases in one oscillation cycle. The LSB corresponds to one over eight of the oscillation period. However, the proposed phase detector employs an interpolation technique to double the phase resolution, thus halving the LSB. By expanding the comparison to ϕ_0 and $\overline{\phi_3}$, ϕ_0 and $\overline{\phi_1}$, ϕ_1 and $\overline{\phi_2}$, and ϕ_2 and $\overline{\phi_3}$, the interpolated phase is detectable, as shown in Fig. 14b. The proposed phase detector utilizes 8 comparator outputs and results in 4 bits resolution. Only four extra comparators and memory are required for the proposed phase detector. Decoding the output of the phase detector is carried out on a host PC after counter and phase values are read out outside the chip. By summing $PHVAL_1$ and $PHVAL_2$, a fine conversion resolution of 5 bits is obtained (corresponding to a LSB of $1.4\ \text{ns}/2^5 = 44$ ps), which, added to the 12 bits of the coarse conversion, corresponds to a total of 17 bits.

4 Characterization

4.1 Chip Fabrication

The sensor chip was fabricated on a 0.35 μm CMOS process, the die size is $4.22 \times 5.24\ \text{mm}^2$. The 4×4 MD-SiPM array occupies $3.2 \times 3.2\ \text{mm}^2$ and each TDC occupies $16 \times 840\ \mu\text{m}^2$ including the readout circuit. A photomicrograph of the MD-SiPM array chip is shown in Fig. 15. The power supply voltage is 3.3 V

(a)

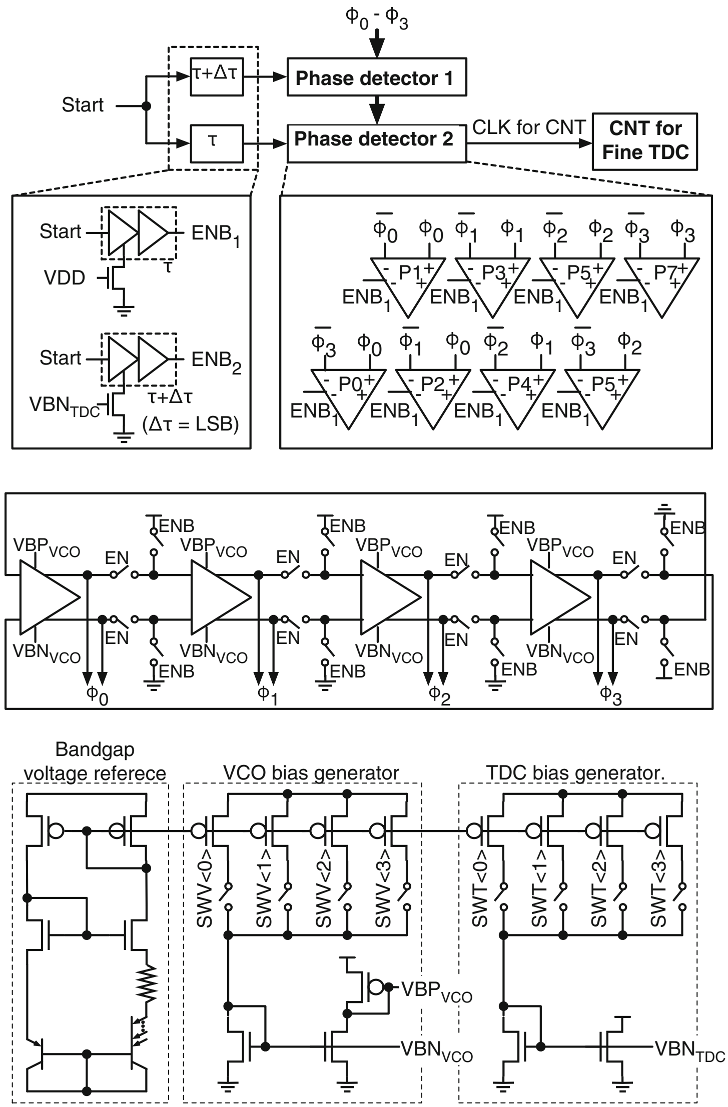

Fig. 13 **a** Schematic of each TDC employing the phase interpolation technique. **b** VCO. **c** Bandgap voltage reference circuit

and the high voltage for SPADs is 22–23 V. The VCO and the bandgap voltage reference consume 80 mA in total, the digital logic 30 mA. The current drawn by each TDC is less than 570 μA, while the MD-SiPM array consumption is 2 mA in the dark. Each SiPM and its fill factor are shown in the figure., along with a denomination. A detail of the SiPM ‘D15’ is shown in the figure, along with the

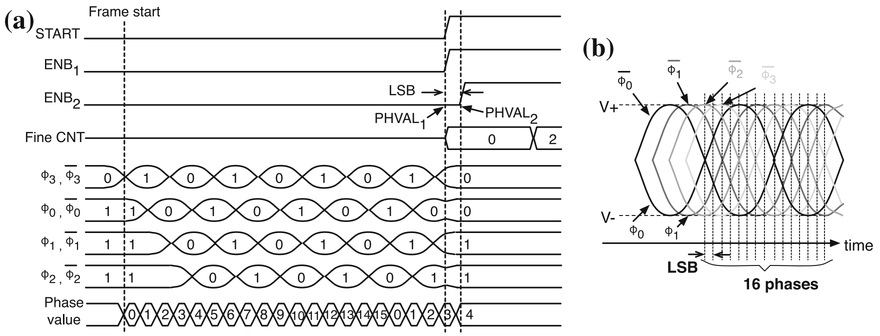

Fig. 14 **a** Timing diagram of the fine TDC. **b** Concept of our proposed phase detector

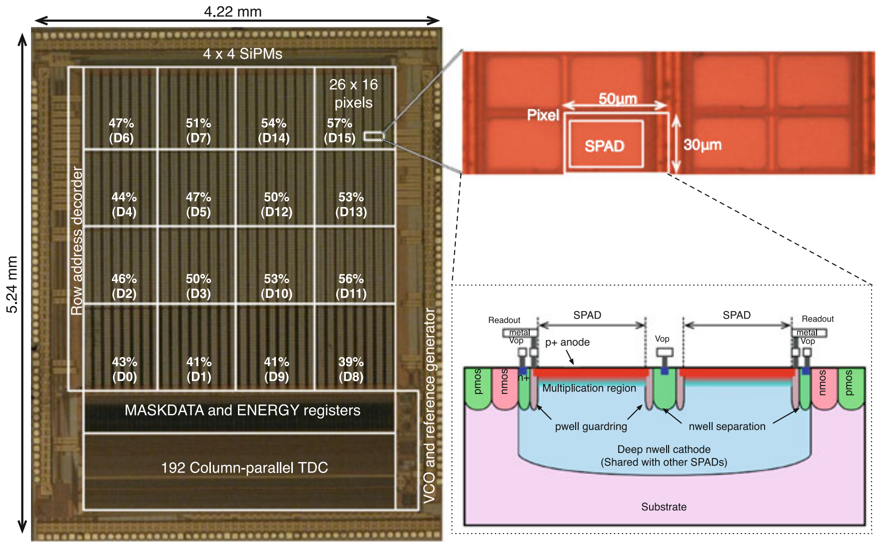

Fig. 15 Chip microphotograph

dimensions of the pixel that achieves a fill factor of 57 %. To maximize fill factor, the electronics was placed at a distance of twice the pitch and implemented in a mirrored fashion.

4.2 Noise and Sensitivity Characterization

Figure 16a shows the cumulative DCR plot for 'D15' SiPM showing the DCR distribution of 416 SPADs for several excess bias voltages and temperatures.

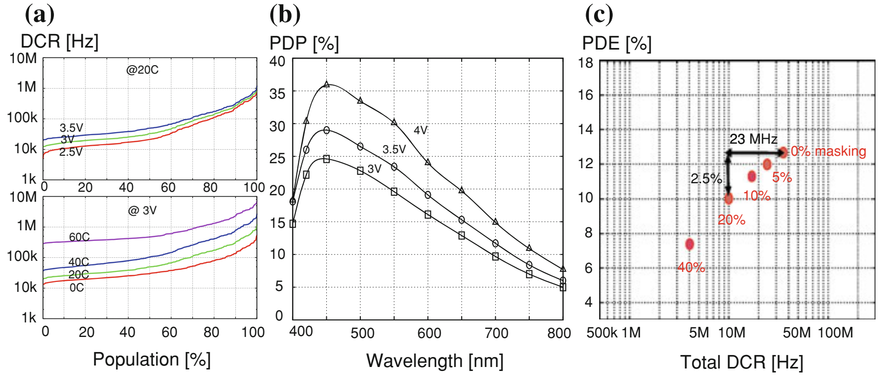

Fig. 16 **a** Cumulative DCR plot for various excess bias voltage and temperature conditions for the 'D15' SiPM. **b** PDP versus wavelength at various excess bias. **c** Relation between DCR and PDE for various SiPMs at 3 V excess bias and 20 °C for several masking levels

The PDP of SPADs is also characterized. We only activate a single SPAD to measure PDP and the dead time of the SPAD is set to be long by using high quenching resistor. Figure 16b shows PDP of a single pixel as a function of wavelength with different excess bias. The temperature dependency of PDP is negligible in the spectral range of interest. The PDP is about 30 % at 4 V excess bias at 420–430 nm which is of interest for TOF PET applications with LYSO scintillators. It means that at most 17.1 % PDE can be achievable by accepting high DCR or by cooling the device. PDE can be calculated based on the PDP measurement results and fill factor by $PDP \times FF$, where FF the fill factor. Masking pixels reduces both DCR and fill factor, and thus PDE. However, the reduction is not linear due to the small percentage of highly noisy pixels (screamers). Thus, small masking levels reduce total DCR in one SiPM faster than PDE, while larger masking has a larger impact on PDE and a smaller impact on total DCR. This mechanism for 'D15' at 3 V excess bias and 20 C can be seen in Fig. 16c.

By using the masking circuitry, optical and electrical crosstalk is measured. Figure 17 shows the DCR map at 4 V excess bias, 30 °C temperature in a section of the MD-SiPM that contains a noisy pixel before (a) and after (b) masking of pixels whose DCR is higher than 1 MHz. Figure 17 also shows the DCR reduction in pixels surrounding the noisy SPAD in 4 × 4 pixels. By turning off the noisy pixel, the DCR decreases approximately 10 % in adjacent pixels as well.

4.3 Column-Parallel TDC Timing Characterization

The TDCs were fully characterized using an electrical input, yielding a single-shot timing uncertainty of 60 ps (FWHM). Figure 18a and b show DNL and INL of a

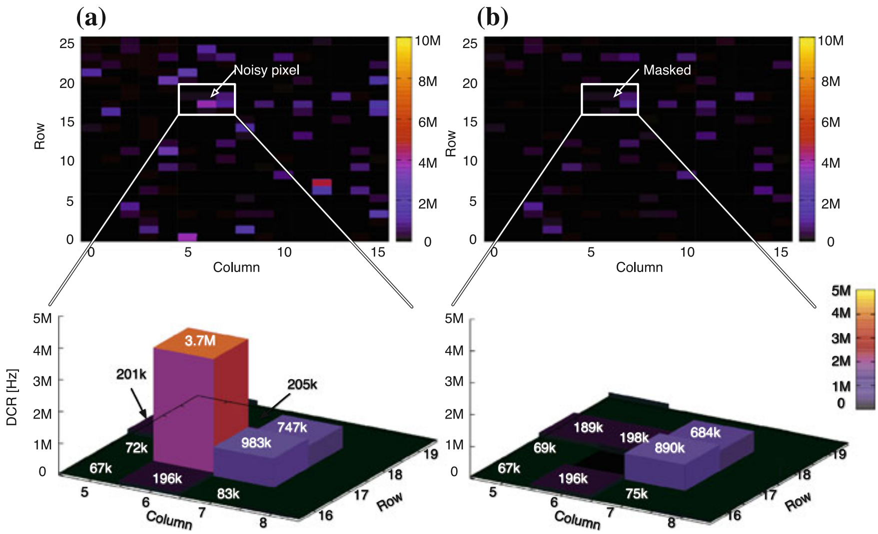

Fig. 17 DCR map (**a**) before masking a noisy SPAD and (**b**) after masking a noisy SPAD. The values in the bottom pictures show the DCR

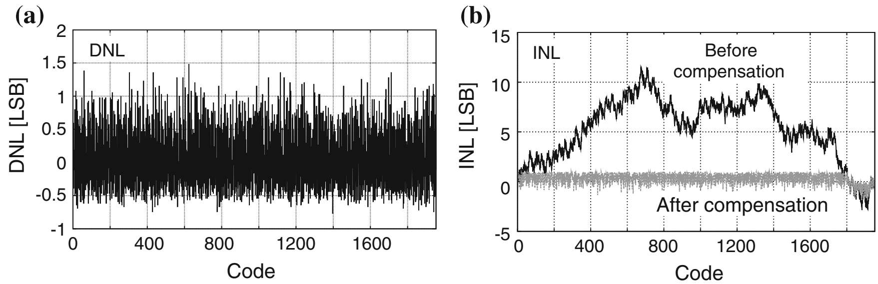

Fig. 18 **a** DNL. **b** INL

typical TDC in the array. Since the INL is mainly caused by the frequency shift of the VCO over the detection period, it can be largely compensated for by means of a lookup table (LUT). Figure 19a summarizes the INL variation for all 192 TDCs after the INL compensation. Figure 19b shows the LSB shift of the TDCs due to temperature and power supply fluctuations. The TDCs suffer from a 6 to 9 % LSB shift in the ±30 °C range and ±10 % power supply variation.

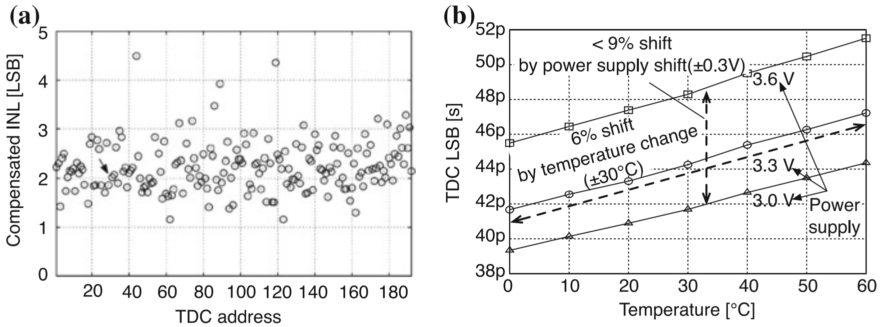

Fig. 19 **a** INL variation after compensation in a TDC when all 192 TDCs are in operation. **b** LSB shift for the TDC due to temperature and power supply fluctuation

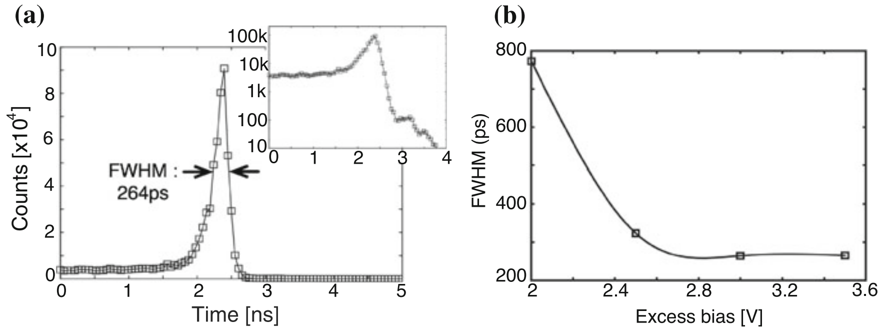

Fig. 20 **a** Single-photon FWHM timing resolution for a single SPAD using a TDC. **b** Single-photon FWHM timing resolution for the complete SiPM at various excess bias voltages

4.4 MD-SiPM Timing Characterization

The timing resolution of 21 % fill factor MD-SiPM was established optically in a TCSPC experiment using a 250 mW, 405 nm laser source (ALDS GmBH) with 40 ps pulse width. Figure 20a shows SPTR measurements of the MD-SiPM. The SPTR of the MD-SiPM is measured with a single-photon level intensity obtained from a laser on average. Asymmetric shape of the count level before and after the laser pulse is due to the fact that a laser intensity is close to one photon per a laser pulse and the relatively high DCR will trigger the MD-SiPM before but not after the laser pulse. The SPTR consists of mainly SPAD jitter, TDC intrinsic jitter, pixel-to-pixel skew of the TDC input lines, and laser jitter. The FWHM timing resolution is 264 ps, including the SPAD jitter, 93.2 ps TDC intrinsic jitter and the pixel-to-pixel skew, when the photon source exhibits 34 ps FWHM jitter. The sensor is operated at 3 V excess bias. Figure 20b shows the FWHM timing resolution as a function of excess bias. The SPTR improves by increasing excess bias for SPADs, because the SPAD jitter dramatically decreases when the excess bias is high.

5 Conclusions

In a PET application, high speed imaging with precise timing information acquisition is required for the gamma detection We have proposed a 4 × 4 array of D-SiPMs capable of timestamping up to 48 photons, denominated multi-channel D-SiPM or MD-SiPM. We have shown the advantage of generating multiple timestamps in the context of PET. The MD-SiPMs have a pitch of 800 m and comprise 416 pixels each; the timing resolution achieved by the SiPMs is 264 ps FWHM, while each pixel has a fill factor of up to 57 % and a single-photon timing resolution of 114 ps. The sensor is the prototype of the core detector of the worlds's first endoscopic digital PET.

References

1. P. E. Valk, D. L. B. D. Delbeke, D. W. Townsend, and M. N. Maisey, *Positron Emission Tomography*. Springer, 2004.
2. M. E. Phelps, *PET Physics, Instrumentation, and Scanners*. Springer, 2006.
3. W. W. Moses, "Time of flight in PET revisited," *IEEE Trans. Nucl. Sci.*, vol. 50, no. 5, pp. 1325–1330, Oct. 2003.
4. M. Conti, "Effect of randoms on singal-to-noise ratio in TOF PET," *IEEE Trans. Nucl. Sci.*, vol. 53, no. 3, pp. 1188–1193, Jun. 2006.
5. M. Conti, "Focus on time-of-flight PET: the benefits of improved time resolution," *Eur. J. Nucl. Med. Mol. I*, vol. 38, no. 6, pp. 1147–1157, Jun. 2011.
6. HAMAMATSU, "MPPC," http://jp.hamamatsu.com, 2013.
7. T. Nagano, K. Sato, A. Ishida, T. Baba, R. Tsuchiya, and K. Yamamoto, "Timing resolution improvement of MPPC for TOF-PET imaging," in *Proc. IEEE Nuclear Science Symp. Conf.*, 2012, pp. 1577–1580.
8. P. Buzhan, B. Dolgoshein, L. Filatov, A. Ilyin, V. Kantzerov, V. Kaplin, A. Karakash, F. Kayumov, S. Klemin, E. Popova, and S. Smirnov, "Silicon photomultiplier and its possible applications," *Nucl. Instrum. Methods Phys. Res. A*, vol. 504, no. 1–3, pp. 48–52, May 2003.
9. A. G. Stewart, V. Saveliev, S. J. Bellis, D. J. Herbert, P. J. Hughes, and J. C. Jackson, "Performance of 1-mm^2 silicon phopomultiplier," *IEEE J. Quantum Electron.*, vol. 44, no. 2, pp. 157–164, Feb. 2008.
10. N. Zorzi, M. Melchiorri, A. Piazza, C. Piemonte, and A. Tarolli, ''Development of large-area silicon photomultiplier detectors for PET applications at FBK,'' *Nucl. Instrum. Methods Phys. Res. A*, vol. 636, no. 1, pp. 208–213, Apr. 2011.
11. M. Mazzillo, G. Condorelli, D. Sanfilippo, G. Valvo, B. Carbone, A. Piana, G. Fallica, A. Ronzhin, M. Demarteau, S. Los, and E. Ramberg, "Timing performances of large area silicon photomultipliers fabricated at STMicroelectronics," *IEEE Trans. Nucl. Sci.*, vol. 57, no. 4, pp. 2273–2279, Aug. 2010.

12. M. McClish, P. Dokhale, J. Christian, C. Stapels, E. Johnson, R. Robertson, and K. S. Shah, "Performance measurements of CMOS position sensitive solid-state photomultipliers," *IEEE Trans. Nucl. Sci.*, vol. 57, no. 4, pp. 2280–2286, Aug. 2010.
13. T. Frach, G. Prescher, C. Degenhardt, R. Gruyter, A. Schmitz, and R. Ballizany, "The digital silicon photomultiplier— principle of operation and intrinsic detector performance," in *Proc. IEEE Nuclear Science Symp. Conf.*, 2009, pp. 1959–1965.
14. T. Frach, G. Prescher, C. Degenhardt, and B. Zwaans, "The digital silicon photomultiplier—system architecture and performance evaluation," in *Proc. IEEE Nuclear Science Symp. Conf.*, 2010, pp. 1722–1727.
15. Y. Haemisch, T. Frach, C. Degenhardt, and A. Thon, "Fully digital arrays of silicon photomultipliers (dSiPM)—a scalable alternative to vacuum photomultiplier tubes (PMT)," in *Proc. of TIPP*, vol. 37, 2011, pp. 1546–1560.
16. D. Tyndall, B. Rae, D. Li, J. Richardson, J. Arlt, and R. Henderson, "A 100 M photon/s time-resolved mini-silicon photomultiplier with on-chip fluorescence lifetime estimation in 0.13 μm CMOS imaging technology," in *IEEE ISSCC Dig. Tech. Papers*, 2012, pp. 122–124.
17. L. Braga, L. Gasparini, L. Grant, R. Henderson, N. Massari, M. Perenzoni, D. Stoppa, and R. Walker, "An 8x16-pixel 92 k SPAD time-resolved sensor with on-pixel 64 ps 12b TDC and 100Ms/s real-time energy histogramming in 0.13 μm CIS technology for PET/MRI applications," in *IEEE ISSCC Dig. Tech. Papers*, 2013, pp. 486–487.
18. J. Glodo, W. W. Moses, W. M. Higgins, E. V. D. van Loef, P. Wong, S. E. Derenzo, M. J. Weber, and K. S. Shah, "Effects of Ce concentration on scintillation properties of $LaBr_3$:Ce," *IEEE Trans. Nucl. Sci.*, vol. 52, no. 5, pp. 1805–1808, Oct. 2005.
19. S. Park, "On the asymptotic fisher information in order statistics," *Metrika*, vol. 57, no. 1, pp. 71–80, 2003.
20. C. Veerappan, J. Richardson, R. Walker, D. U. Li, M. W. Fishburn, Y. Maruyama, D. Stoppa, F. Borghetti, M. Gersbach, R. K. Henderson, and E. Charbon, "A 160 $\times$ 128 single-photon image sensor with on-pixel 55 ps 10b time-to-digital converter," in *IEEE ISSCC Dig. Tech. Papers*, 2011, pp. 312–314.
21. S. Mandai and E. Charbon, "Timing optimization of a H-tree based digital silicon photomultiplier," *Journal of Instrum.*, vol. 8, no. 9, pp. 1–7, 2013.
22. S. Mandai and E. Charbon, "A multi-channel digital silicon photomultiplier array for nuclear medical imaging systems based on PET-MRI," *Proc. IISW*, 2013.
23. S. Mandai, V. Jain, and E. Charbon, "A 780 $\times$ 800 μm^2 multi-channel digital silicon photomultiplier with column-parallel time-to-digital converter and basic characterization," *IEEE Trans. Nucl. Sci.*, vol. 52, no. 10, pp. 1805–1808, Oct. 2014.
24. C. Degenhardt, G. Prescher, T. Frach, A. Thon, R. de Gruyter, A. Schmitz, and R. Ballizany, "The digital silicon photomultiplier—a novel sensor for the detection of scintillation light," in *Proc. IEEE Nuclear Science Symp. Conf.*, 2009, pp. 2383–2386.